

HERMES: SPATIALLY RESOLVED ALMA IMAGING OF HERSCHEL[†]-SELECTED DUSTY STAR-FORMING GALAXIES

R. S. BUSSMANN¹, D. RIECHERS¹

To be submitted to the ApJ

ABSTRACT

The *Herschel* Multi-tiered Extragalactic Survey (HerMES) has identified large numbers of dusty star-forming galaxies (DSFGs) over a wide range in redshift. A detailed understanding of these DSFGs is hampered by the poor spatial resolution of *Herschel*. We present 870 μm 0''.45 imaging obtained in Cycle 0 with the Atacama Large Millimeter Array (ALMA) of a sample of 29 HerMES DSFGs. We identify a total of 62 sources down to the 5 σ limit in our ALMA sample ($\sigma \approx 0.2 \text{ mJy}$). Optical or near-infrared imaging indicates that 36 of the ALMA sources experience a significant flux boost from gravitational lensing ($\mu > 1.1$), but only 5 are strongly lensed and show multiple images. This finding corroborates evidence from brighter *Herschel* DSFGs that a simple Schechter function fails to accurately represent the bright end of the DSFG luminosity function. We introduce and make use of a general purpose and publicly available Markov Chain Monte Carlo visibility plane analysis tool to analyze the source properties. *Results 1: distribution of intrinsic fluxes and observed fluxes. Results 2: distribution of projected separations between ALMA sources and comparison to Hayward+13 and similar paper from Durham group in 2014. Results 3: Distribution of angular sizes and ellipticities. and of course any other ideas we might have.*

Keywords: galaxies: evolution — galaxies: fundamental parameters — galaxies: high-redshift

1. INTRODUCTION

Galaxies selected in blind surveys at far-infrared (far-IR) or sub-millimeter (sub-mm) wavelengths are generally known as dusty star-forming galaxies (DSFGs). They are found primarily at $z \sim 2$ (Chapman et al. 2005) and represent the most luminous objects in existence during this epoch. They are signposts of significant over-densities and likely represent the formative stages of the most massive elliptical galaxies found in the local Universe (e.g., Ivison et al. 2013; Fu et al. 2013). Moreover, they constitute an important component of the overall galaxy population at $z \sim 2$ (e.g., Le Floc'h et al. 2005), when the star-formation rate density in the Universe peaked (e.g., Madau et al. 1996).

Our collective understanding of DSFGs is currently taking a dramatic leap forward thanks in large part to the advent of the *Herschel Space Observatory* (*Herschel*; Pilbratt et al. 2010). This has resulted in a revolution in the size and depth of blind surveys at far-IR and sub-mm wavelengths. In particular, the *Herschel* Multi-tiered Extragalactic Survey (HerMES; Oliver et al. 2012) and the *Herschel* Astrophysical Terahertz Large Area Survey (H-ATLAS; Eales et al. 2010) together have surveyed $\approx 650 \text{ deg}^2$ at 250 μm , 350 μm , and 500 μm to the confusion limit ($\sigma \approx 6 - 7 \text{ mJy}$ in each band Nguyen et al. 2010), plus an additional $\approx 350 \text{ deg}^2$ to a level approximately double the confusion limit.

Theoretical expectations based on the redshift distribution and luminosity function of DSFGs suggested that HerMES and H-ATLAS would be efficient tools for discovering strongly lensed DSFGs (e.g., Blain 1996; Ne-

grello et al. 2007). Submillimeter Array (SMA; Ho et al. 2004) imaging at 870 μm with sub-arcsecond resolution has confirmed this, with $\geq 85\%$ of the brightest sources found by *Herschel* ($S_{500} > 100 \text{ mJy}$) being gravitationally lensed by an intervening galaxy or group of galaxies along the line of sight (Negrello et al. 2010; Wardlow et al. 2013; Bussmann et al. 2013). However, statistical models significantly over-predict the median magnification factor experienced by a *Herschel* DSFG of a given S_{500} (Bussmann et al. 2013). This could indicate a deficiency in our understanding of the bright end of the intrinsic DSFG luminosity function.

To investigate this further, we obtained Atacama Large Millimeter/submillimeter Array (ALMA) Cycle 0 imaging at 870 μm of a sample of 29 HerMES DSFGs. Three aspects of our dataset make it unique. First, the sample occupies a distinct regime in flux density between the brightest *Herschel* DSFGs (almost all of which are lensed) and much fainter DSFGs found in ground-based surveys (most of which are expected to be unlensed; e.g., Hodge et al. 2013). Second, the ALMA images are extremely sensitive ($\sigma \approx 0.2 \text{ mJy}$) and all 29 HerMES DSFGs are detected. Third, the typical angular resolutions are 0''.45 and nearly all sources detected by ALMA are spatially resolved.

We also obtained Gemini-South optical imaging to complement our existing array of ancillary multi-wavelength imaging. We use those data in this paper to identify lensing galaxies which are typically early-types with little on-going star-formation and therefore very weak sub-mm emission.

In Section 2, we characterize our sample and present our ALMA and Gemini-South imaging. Section 3 presents model fitting methodology and model fits to all ALMA sources (lensed and unlensed) using UVMCMCFIT,

[†] *Herschel* is an ESA space observatory with science instruments provided by European-led Principal Investigator consortia and with important participation from NASA.

¹ Department of Astronomy, Space Sciences Building, Cornell University, Ithaca, NY, 14853-6801

a publicly available³ software tool that we created that is a modified version of the visibility plane lens modeling software used in Bussmann et al. (2013). Results on the effect of lensing on the observed properties of the *Herschel* DSFGs in our sample as well as the multiplicity rate and typical angular separation between sources after delensing the ALMA sources appear in Section 4. We scrutinize statistical predictions for μ_{870} as a function of S_{870} and discuss implications for the bright end of the DSFG luminosity function in Section 5. Finally, we present our conclusions in Section 6.

Throughout this paper, we assume a flat cosmology with $H_0 = 69 \text{ km s}^{-1} \text{ Mpc}^{-1}$, $\Omega_{\text{m}_0} = 0.29$.

2. DATA

In this section, we describe the selection of our *Herschel* DSFG sample, present our ALMA high-spatial resolution imaging of thermal dust emission, and present Gemini-S optical imaging that we use to identify intervening galaxies along the line of sight.

2.1. Selection of DSFG Sample

The starting point for the sample selection is source extraction and photometry. Sources are detected using the STARFINDER code (Diolaiti et al. 2000) on the $250 \mu\text{m}$ *Herschel* Spectral and Photometric Imaging REceiver (SPIRE; Griffin et al. 2010) images. Photometry is obtained from the HerMES XID pipeline (Roseboom et al. 2010), which allocates flux density based on the $250 \mu\text{m}$ position priors from STARFINDER.

Our sample includes 29 DSFGs drawn from five independent fields in HerMES totaling 55 deg^2 that are accessible to ALMA and have SPIRE sensitivity that reaches the confusion limit. The sample is selected primarily on the basis of S_{500} and covers a range of $20 < S_{500}/(\text{mJy}) \lesssim 100$. Low redshift interlopers ($z < 0.1$) are trivially removed from the sample by searching for spatially resolved counterparts in SDSS imaging. There is also a small contamination from blazars, which are non-thermal emitters and are easily removed using data from the NVSS or the Very Large Array Faint Images of the Radio Sky at Twenty-Centimeters survey (FIRST; Becker et al. 1995).

Figure 1 shows that the ALMA sample is set clearly apart from the very bright *Herschel* DSFGs that are selected to have $S_{500} > 100 \text{ mJy}$ and have been shown to be almost completely uncontaminated by unlensed DSFGs (Negrello et al. 2010; Wardlow et al. 2013; Bussmann et al. 2013). In contrast, the sample in this paper should include a larger mix of unlensed DSFGs. On the other hand, this sample is selected from a survey with an area that is 200 times larger than that of ALESS. It is no surprise then, that the median S_{500} in our sample is ~ 3.5 times brighter than the median S_{500} in ALESS. Our ALMA sample opens a new window of discovery space on the bright end of the DSFG luminosity function.

In detail, two of the sources in the ALMA sample (HXMM01 and HXMM02) overlap with the “confirmed lensed” sample in Wardlow et al. (2013) as well as with the SMA sample in Bussmann et al. (2013). A further 8 appear in the “Supplementary sample” in Wardlow et al.

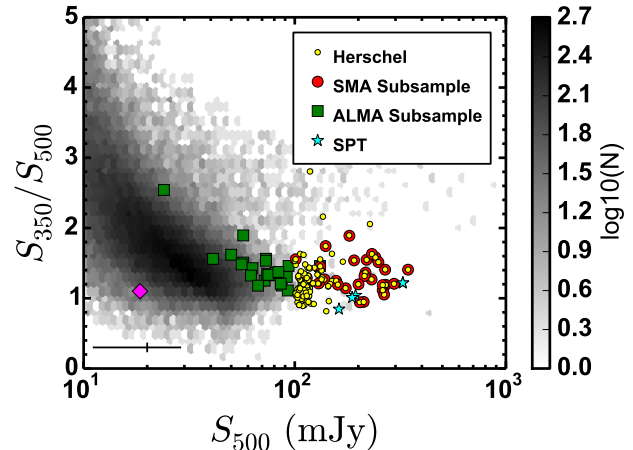


Figure 1. *Herschel*/SPIRE photometry of all galaxies in the H-ATLAS phase I catalog with $S/N > 3$ at $250 \mu\text{m}$, $350 \mu\text{m}$, and $500 \mu\text{m}$ (grayscale). The sample of HerMES sources in this paper are shown with green squares (the “ALMA sample”). The very bright *Herschel* DSFGs from Bussmann et al. (2013) (the “SMA sample”) are shown by red circles, and the overall sample of candidate lensed *Herschel* DSFGs are highlighted by yellow circles. Lensed SMGs discovered by the SPT that have published lens models are represented by cyan stars (Hezaveh et al. 2013). A magenta diamond shows the location in this diagram of the stacked signal from ALESS DSFGs. Representative error bars are shown in the lower left corner. The ALMA sample fills the gap in $500 \mu\text{m}$ flux density space between SMA/SPT and ALESS samples.

(2013). The remainder have $S_{500} < 80 \text{ mJy}$ and thus do not appear in Wardlow et al. (2013).

Table 1 provides basic positional data for the ALMA sample, including the International Astronomical Union addresses (for the full IAU name, prepend “1HerMES 250” to the IAU address), short names to aid comparison with previous publications, centroid positions measured from the ALMA $870 \mu\text{m}$ imaging (see section 2.2), and redshift measurements for the lens(es) and sources, where available.

³ <https://github.com/sbussmann/uvmcmcfit>

Table 1
Observed positions and flux densities of ALMA sources. Uncertainties in flux densities do not include absolute calibration uncertainty of $\approx 10\%$.

IAU address ^a	Short name	RA ₈₇₀ (J2000)	Dec ₈₇₀ (J2000)	S_{250} (mJy)	S_{350} (mJy)	S_{500} (mJy)	S_{870} (mJy)	Lens Grade
J045057.5-531654	ADFS01	04:50:57.715	-53:16:54.42	138 \pm 6	114 \pm 6	73 \pm 6	10.41 \pm 0.44	—
	Source0	04:50:57.610	-53:16:55.09	—	—	—	6.68 \pm 0.28	C
	Source1	04:50:57.805	-53:16:56.96	—	—	—	1.98 \pm 0.18	C
	Source2	04:50:57.741	-53:16:54.54	—	—	—	1.75 \pm 0.26	C
J045026.5-524127	ADFS02	04:50:27.453	-52:41:25.41	88 \pm 6	81 \pm 6	50 \pm 6	10.39 \pm 0.42	—
	Source0	04:50:27.092	-52:41:25.62	—	—	—	5.56 \pm 0.23	C
	Source1	04:50:27.806	-52:41:25.10	—	—	—	4.83 \pm 0.35	X
	ADFS03	04:49:46.448	-52:54:26.95	115 \pm 6	61 \pm 6	24 \pm 6	13.39 \pm 0.49	—
J044946.9-525424	Source0	04:49:46.603	-52:54:23.66	—	—	—	7.50 \pm 0.24	X
	Source1	04:49:46.301	-52:54:30.26	—	—	—	3.84 \pm 0.27	X
	Source2	04:49:46.280	-52:54:26.06	—	—	—	2.06 \pm 0.30	X
	ADFS04	04:41:03.942	-53:12:41.01	96 \pm 6	86 \pm 6	57 \pm 6	14.94 \pm 0.33	—
J044103.8-531240	Source0	04:41:03.866	-53:12:41.33	—	—	—	8.65 \pm 0.23	X
	Source1	04:41:04.000	-53:12:40.10	—	—	—	3.53 \pm 0.18	X
	Source2	04:41:03.912	-53:12:42.09	—	—	—	2.76 \pm 0.16	X
	ADFS05	04:36:19.702	-55:24:25.01	110 \pm 6	102 \pm 6	87 \pm 6	15.29 \pm 0.37	—
J043619.3-552425	Source0	04:36:19.706	-55:24:24.41	—	—	—	7.02 \pm 0.42	X
	Source1	04:36:19.698	-55:24:25.27	—	—	—	8.27 \pm 0.53	X
	ADFS06	04:33:40.450	-54:03:39.51	76 \pm 6	90 \pm 6	72 \pm 6	17.94 \pm 0.50	—
	Source0	04:33:40.455	-54:03:40.29	—	—	—	9.07 \pm 0.27	C
J043340.5-540337	Source1	04:33:40.501	-54:03:40.05	—	—	—	6.08 \pm 0.32	C
	Source2	04:33:40.472	-54:03:38.33	—	—	—	2.79 \pm 0.27	C
	ADFS07	04:41:53.880	-54:03:53.48	80 \pm 6	103 \pm 6	93 \pm 6	32.36 \pm 0.64	A
	ADFS_M0	04:38:30.883	-54:18:29.38	57 \pm 6	78 \pm 5	75 \pm 6	20.59 \pm 0.48	—
J043829.7-541831	Source0	04:38:30.780	-54:18:31.79	—	—	—	14.00 \pm 0.40	C
	Source1	04:38:30.970	-54:18:26.60	—	—	—	6.59 \pm 0.28	C
	CDFDS_M0	03:27:52.011	-29:09:10.40	28 \pm 7	84 \pm 6	85 \pm 6	33.16 \pm 0.45	—
	Source0	03:27:52.002	-29:09:12.07	—	—	—	13.07 \pm 0.40	A
J032752.0-290908	Source1	03:27:52.002	-29:09:09.65	—	—	—	14.26 \pm 0.22	C
	Source2	03:27:52.025	-29:09:12.14	—	—	—	5.83 \pm 0.11	X
	CDFDS_M1	03:32:10.840	-27:05:34.18	73 \pm 6	86 \pm 6	85 \pm 6	13.12 \pm 0.25	—
	Source0	03:32:10.905	-27:05:32.87	—	—	—	10.54 \pm 0.24	C
J033317.9-280907	Source1	03:32:10.729	-27:05:36.22	—	—	—	2.58 \pm 0.11	C
	ECDFS02	03:33:18.017	-28:09:07.52	96 \pm 6	90 \pm 6	63 \pm 6	14.13 \pm 0.25	—
	Source0	03:33:18.006	-28:09:07.55	—	—	—	9.30 \pm 1.20	X
	Source1	03:33:18.032	-28:09:07.39	—	—	—	4.83 \pm 1.26	X
J100144.1+025712	COS01	10:01:44.182	+02:57:12.47	91 \pm 6	100 \pm 6	74 \pm 6	12.82 \pm 0.39	A
J100056.6+022014	COS02	10:00:57.180	+02:20:12.70	71 \pm 6	64 \pm 6	41 \pm 6	10.37 \pm 0.51	—
J003823.6-433707	Source0	10:00:56.946	+02:20:17.35	—	—	—	3.31 \pm 0.16	X
	Source1	10:00:57.565	+02:20:11.26	—	—	—	2.26 \pm 0.19	X
	Source2	10:00:56.855	+02:20:08.93	—	—	—	1.54 \pm 0.23	X
	Source3	10:00:57.274	+02:20:12.66	—	—	—	1.45 \pm 0.18	X
J003823.6-433707	Source4	10:00:57.400	+02:20:10.83	—	—	—	1.80 \pm 0.33	X
	ElaiaS1	00:38:23.587	-43:37:04.15	114 \pm 6	101 \pm 6	76 \pm 6	17.20 \pm 0.44	—
	Source0	00:38:23.762	-43:37:06.10	—	—	—	8.85 \pm 0.21	C
	Source1	00:38:23.482	-43:37:05.56	—	—	—	3.76 \pm 0.19	C
J022016.5-060143	Source2	00:38:23.313	-43:36:58.97	—	—	—	2.84 \pm 0.23	C
	Source3	00:38:23.803	-43:37:10.46	—	—	—	1.75 \pm 0.20	X
	XMM01	02:20:16.609	-06:01:43.18	180 \pm 7	192 \pm 8	132 \pm 7	25.09 \pm 0.51	—
	Source0	02:20:16.648	-06:01:41.93	—	—	—	13.77 \pm 0.34	C
J022201.6-033340	Source1	02:20:16.571	-06:01:44.56	—	—	—	10.56 \pm 0.37	C
	Source2	02:20:16.609	-06:01:40.72	—	—	—	0.76 \pm 0.32	C
	XMM02	02:22:01.616	-03:33:41.40	107 \pm 7	108 \pm 8	81 \pm 7	11.57 \pm 0.56	—
	Source0	02:22:01.592	-03:33:39.42	—	—	—	8.45 \pm 0.38	C
J022548 -041750	Source1	02:22:01.629	-03:33:43.58	—	—	—	3.12 \pm 0.41	X
	XMM03	02:25:47.942	-04:17:50.80	106 \pm 7	119 \pm 8	92 \pm 7	14.73 \pm 0.35	C
	XMM04	02:18:53.111	-06:33:24.65	89 \pm 7	83 \pm 7	56 \pm 7	7.25 \pm 0.44	—
	Source0	02:18:53.118	-06:33:24.19	—	—	—	5.46 \pm 0.30	C
J023006.0-034152	Source1	02:18:53.095	-06:33:25.21	—	—	—	1.78 \pm 0.37	C
	XMM05	02:30:05.950	-03:41:53.07	102 \pm 7	110 \pm 8	81 \pm 7	16.34 \pm 0.37	C
	XMM06	02:18:30.673	-05:31:31.75	92 \pm 7	122 \pm 8	113 \pm 7	62.06 \pm 0.57	A
	XMM16	02:21:34.891	-06:26:17.87	121 \pm 7	132 \pm 8	110 \pm 7	188 \pm 0.41	C
J022201.6-033340	XMM101	02:22:50.573	-03:24:12.35	97 \pm 7	82 \pm 7	62 \pm 7	8.77 \pm 0.24	C
	XMM102	02:19:42.783	-05:24:34.84	85 \pm 7	79 \pm 7	67 \pm 7	14.21 \pm 0.61	—
	Source0	02:19:42.629	-05:24:37.11	—	—	—	5.15 \pm 0.32	X
	Source1	02:19:42.838	-05:24:35.11	—	—	—	3.31 \pm 0.39	X
J022135.1-062617	Source2	02:19:42.769	-05:24:36.48	—	—	—	2.88 \pm 0.22	X
	Source3	02:19:42.682	-05:24:36.82	—	—	—	1.94 \pm 0.37	X
	Source4	02:19:42.955	-05:24:32.22	—	—	—	0.94 \pm 0.18	X
	XMM108	02:19:18.417	-03:10:51.35	91 \pm 7	104 \pm 8	86 \pm 7	29.16 \pm 0.58	A
J022944.7-034110	XMM109	02:29:44.740	-03:41:09.57	90 \pm 7	100 \pm 7	75 \pm 7	23.13 \pm 0.41	—
	Source0	02:29:44.701	-03:41:09.29	—	—	—	19.62 \pm 0.27	C
	Source1	02:29:44.793	-03:41:09.92	—	—	—	3.51 \pm 0.30	C

Table 1 — *Continued*

IAU address ^a	Short name	RA ₈₇₀ (J2000)	Dec ₈₇₀ (J2000)	S_{250} (mJy)	S_{350} (mJy)	S_{500} (mJy)	S_{870} (mJy)	Lens Grade
J021841.5-035002	XMM110	02:18:41.613	-03:50:03.70	128 ± 7	112 ± 7	73 ± 7	10.13 ± 0.43	—
—	Source0	02:18:41.520	-03:50:04.72	—	—	—	6.31 ± 0.34	X
—	Source1	02:18:41.700	-03:50:02.57	—	—	—	3.81 ± 0.25	C
J022021.7-015328	XMM115	02:20:21.756	-01:53:30.92	144 ± 7	137 ± 8	93 ± 11	17.61 ± 0.49	C
J022029.2-064845	XMM119	02:20:29.140	-06:48:46.49	120 ± 7	115 ± 8	84 ± 7	14.46 ± 0.37	—
—	Source0	02:20:29.195	-06:48:48.02	—	—	—	8.47 ± 0.30	C
—	Source1	02:20:29.079	-06:48:44.86	—	—	—	5.98 ± 0.18	C
J022205.4-070728	XMM124	02:22:05.362	-07:07:28.10	137 ± 7	108 ± 7	57 ± 7	2.75 ± 0.14	X

^a IAU name = 1HerMES S250 + IAU address

2.2. ALMA Observations

ALMA data were obtained during Cycle 0 over a period from 2012 June to 2012 December (Program 2011.0.00539.S; PI: D. Riechers). The observations were carried out in good 870 μ m weather conditions which resulted in typical system temperatures of $T_{\text{sys}} \sim 130$ K and phase fluctuations of ~ 10 deg. Each target was observed until an rms noise level of $\sigma \approx 0.2$ mJy was achieved. This typically required 10 minutes of on-source integration time. The number of antennas used varied from 15 to 25. The antennas were configured with baseline lengths of 20 m to 400 m, providing a synthesized beamsize of $\approx 0''.45$ FWHM while ensuring that no flux was resolved out by the interferometer. When possible, track-sharing of multiple targets in a single track was used to optimize the *uv* coverage.

The quasars J0403–360, J2258–279, B0851+202, and J2258–279 were used for bandpass and pointing calibration. The quasars J0403–360, J0106–405, J0519–454, J1008+063, and J0217+017 were used for amplitude and phase gain calibration. The following solar system objects were used for absolute flux calibration: Callisto (CDFS targets), Neptune (XMM targets), Titan (COSMOS targets) and Uranus (ADFS and XMM targets). For ElaisS1, no solar system object was observed. Instead, J2258–279 was used for absolute flux calibration, with the flux fixed according to a measurement made two days prior to the observations of ElaisS1.

All observations were conducted with the correlator in “Frequency Domain Mode”, providing a total usable bandwidth of 7.5 GHz with spectral windows centered on 335.995 GHz, 337.995 GHz, 345.995 GHz, 347.996 GHz. We searched for evidence of serendipitous spectral lines but found none.

We used the Common Astronomy Software Applications (CASA, version 4.2.1) package to investigate the quality of the reduced data provided by the North American ALMA Science Center (NAASC). Overall, the quality of the processed data from the NAASC was very high. We achieved a significant improvement in the case of the ADFS and XMM targets by excluding datasets with moderate T_{sys} and poor phase fluctuations. For a handful of targets with peak signal-to-noise ratio (S/N) greater than 20, we obtained a $\approx 10\%$ improvement in S/N by using the CASA SELFCAL task to improve the phase gain corrections. Finally, we updated the absolute flux calibration to use the Butler-JPL-Horizons 2012 solar system models.

For imaging, we used the CASA CLEAN task with Briggs weighting and robust = +0.5 to achieve the optimal balance between sensitivity and spatial resolution. We selected the multi-frequency synthesis option to optimize *uv* coverage. We designed custom masks for each target in CASA to ensure that only regions with high S/N were considered during the cleaning process.

Figure 2 presents our ALMA images (colorscale) in comparison to the *Herschel* SPIRE images (black-white contours) originally used to select the targets and noted in each panel as either 250 μ m or 350 μ m. Each panel is centered on the phase center of the ALMA observations of that target and a white circle traces the FWHM of the primary beam of an ALMA 12 m antenna at 870 μ m. A white dashed box represents the region of each image that is shown in greater detail in Figure 3.

In most targets, the peak of the SPIRE map is spatially coincident with the location of the ALMA sources. In one case where two ALMA sources are separated by $\approx 10''$ (ADFS02), the elongation in the SPIRE 250 μ m map is consistent with the angular separation of the two ALMA counterparts. Otherwise, the SPIRE imaging is consistent with a single component located at the centroid of the ALMA sources. This result is not a surprise, given the typical angular separation of the ALMA sources ($\lesssim 5''$) and the FWHM of the SPIRE beam at 250 μ m (18.1'').

2.3. Gemini-South Imaging

Optical imaging observations using the Gemini Multi-Object Spectrograph-South (GMOS-S; Hook et al. 2004) were conducted in queue mode during the 2013B semester as part of program GS-2013B-Q-77 (PI: R. S. Bussmann). The goal of the program is to use shallow *u*, *g*, *r*, *i*, and *z* imaging to identify structure at $z < 1$ and determine which of the ALMA sources are affected by gravitational lensing. Some of the ALMA sources lie in regions with existing deep optical imaging thanks to the extensive HerMES multi-wavelength dataset — these were excluded from our Gemini-S program. The remaining targets are: ADFS01, ADFS02, ADFS03, ADFS04, ADFS05, ADFS06, ADFS07, ADFS_M0, ElaisS1, XMM02, XMM05, XMM101, XMM108, XMM109, and XMM115. Each of these targets were observed for a total of 9 minutes of on-source integration time in each of *u*, *g*, *r*, *i*, and *z*. The observations were obtained during dark time in with adequate seeing conditions (image quality = 85% $\approx 1.1''$).

The data were reduced using the standard IRAF Gemini GMOS reduction routines, following the standard GMOS-S reduction steps in the example taken from the

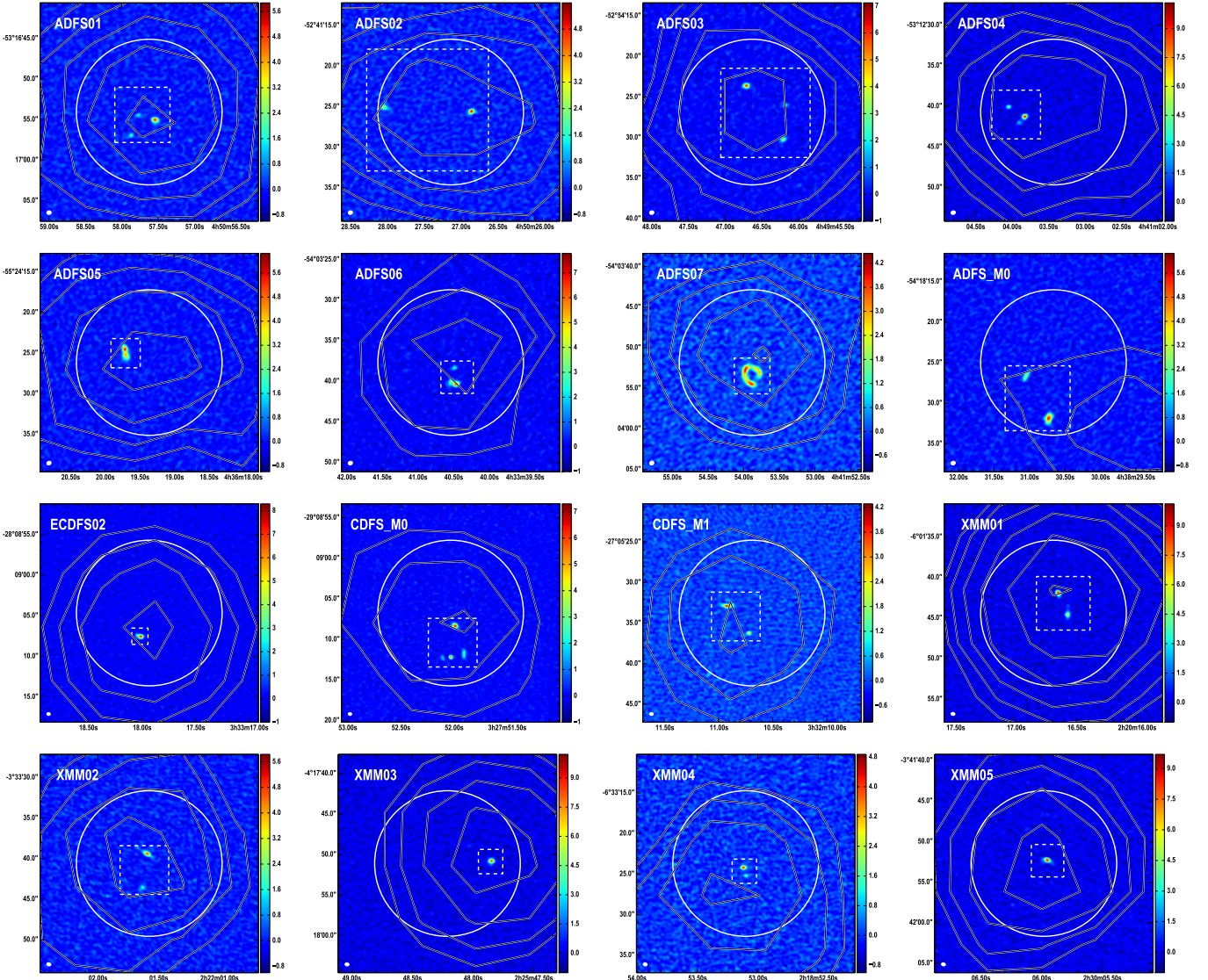


Figure 2. ALMA 870 μm images (color scale, units of mJy/beam) of HerMES DSFGs. Contours (black and white) trace 250 μm emission from *Herschel*. The FWHM size of the ALMA synthesized beam is shown in the lower left corner of each panel. A solid white circle shows the FWHM size of the primary beam. Dashed squares identify the regions of each image that are shown in greater detail in Figure 3.

Gemini observatory webpage⁴.

We used the Sloan Digital Sky Survey (SDSS) or the 2 Micron All Sky Survey (2MASS) to align the Gemini-S images to a common astrometric frame of reference. This imposes an rms uncertainty in the absolute astrometry of 0.² and 0.⁴ for SDSS and 2MASS, respectively. The astrometrically calibrated Gemini-S images served as the basis for aligning higher resolution, smaller field-of-view imaging from *HST* or Keck that were originally presented in Calanog et al. (2014).

3. MODEL FITS

3.1. Model Fitting Methodology

An interferometer measures visibilities at discrete points in the *uv* plane. This is why pixel-to-pixel errors in the inverted and deconvolved surface brightness map of an astronomical source are correlated. The best

way to deal with this situation is to compare model and data visibilities rather than surface brightness maps. The methodology used in this paper is similar in many aspects to that used in Bussmann et al. (2012), who presented the first lens model derived from a visibility-plane analysis of interferometric imaging of a strongly lensed DSFG discovered in wide-field submm surveys as well Bussmann et al. (2013), who extended the work of Bussmann et al. (2012) to a statistically significant sample of 30 objects. It also bears some resemblance to the method used in Hezaveh et al. (2013), who undertake lens modeling of interferometric data in the visibility plane. We summarize important information on the methodology here, taking care to highlight where any differences occur between this work and that of our previous efforts.

We created and made publicly available custom software, called *UVMCMCFIT*, that is capable of modeling all of the ALMA sources in this paper efficiently and reliably.

Sources are assumed to be elliptical Gaussians that

⁴ <http://www.gemini.edu/sciops/data-and-results/processing-software/getting-started#gmos>

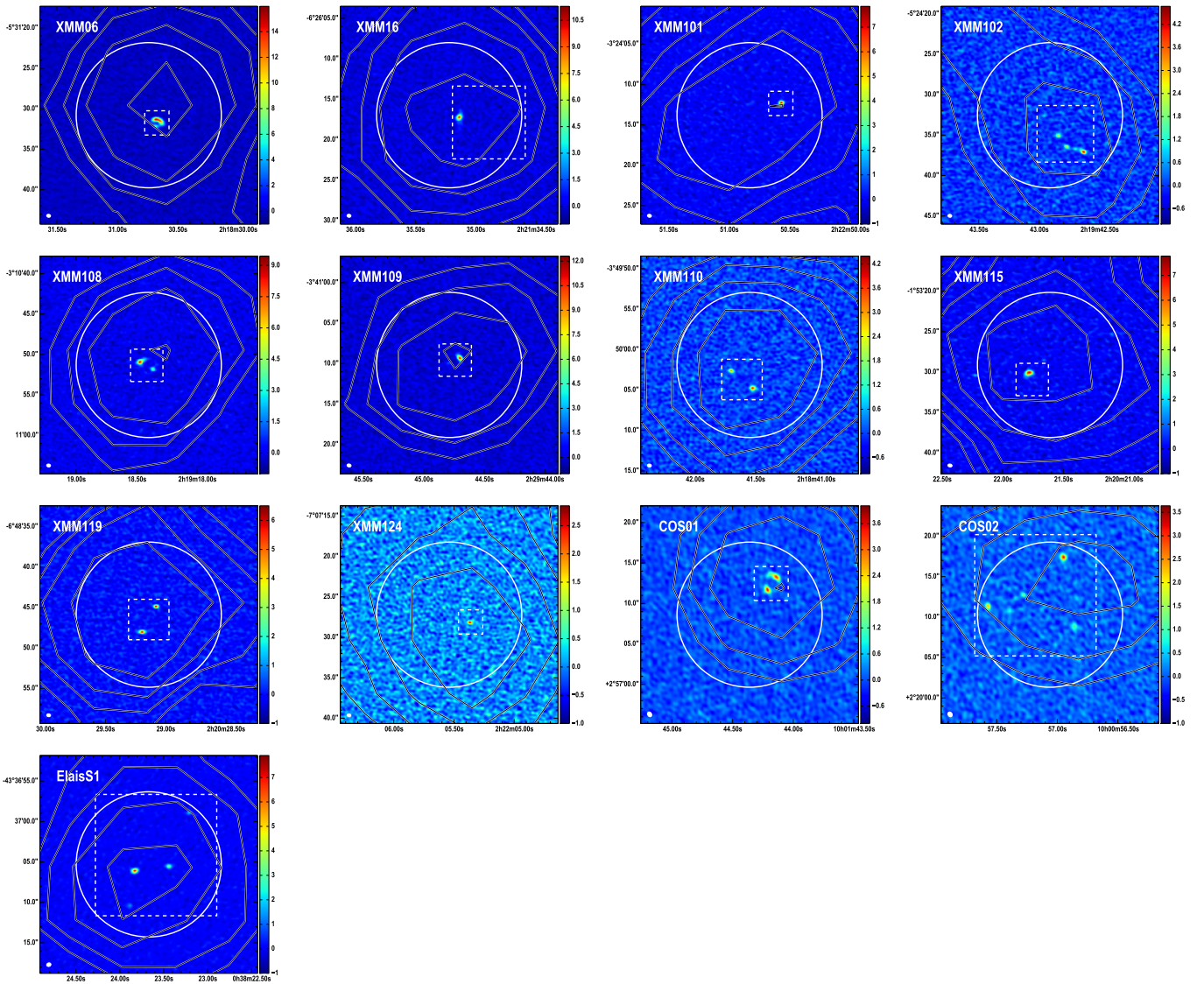


Figure 2. Continued.

are parameterized by the following six free parameters: the position of the source (relative to the primary lens if a lens is present) ($\Delta\alpha_s$ and $\Delta\delta_s$), the total intrinsic flux density (S_{in}), the effective radius intermediate axis length ($r_s = \sqrt{a_s b_s}$), the axial ratio ($q_s = b_s/a_s$), and the position angle (ϕ_s , degrees east of north). The use of an elliptical Gaussian represents a simplification from the Sérsic profile (Sersic 1968) that is justified based on the relatively weak constraints on the Sérsic index found in our previous work (Bussmann et al. 2012, 2013).

When an intervening galaxy (or group of galaxies) is present along the line of sight, UVMCMCFIT accounts for the deflection of light caused by this structure using a simple ray-tracing routine that is adopted from a simple Python routine written by A. Bolton⁵. This represents a significant difference from Bussmann et al. (2012) and Bussmann et al. (2013), where we used the publicly available GRAVLENS software (Keeton 2001) to map emission from the source plane to the image plane for a given lens-

ing mass distribution. GRAVLENS has a wide range of lens mass profiles as well as a sophisticated algorithm for mapping source-plane emission to the image-plane, but it also comes with a significant input/output penalty that makes parallel computing prohibitively expensive. The use of pure-Python code for tracing the deflection of light rays is a critical component of making UVMCMCFIT computationally feasible.

In UVMCMCFIT, lens mass profiles are represented by N_{lens} singular isothermal ellipsoid (SIE) profiles, where N_{lens} is the number of lensing galaxies found from the best available optical or near-IR imaging (a multitude of evidence supports the SIE as a reasonable choice; for a recent review, see Treu 2010). Each SIE is fully described by the following five free parameters: the position of the lens relative to the arbitrarily chosen “image center” based on the ALMA 870 μ m emission and any lensing galaxies seen in the optical or near-IR ($\Delta\alpha_{lens}$ and $\Delta\delta_{lens}$; these can be compared with the position of the optical or near-IR counterpart relative to the “image center”: $\Delta\alpha_{NIR}$ and $\Delta\delta_{NIR}$), the mass of the lens (parame-

⁵ http://www.physics.utah.edu/~bolton/python_lens_demo/

terized in terms of the intermediate axis angular Einstein radius, θ_E), the axial ratio of the lens ($q_{\text{lens}} = b_{\text{lens}}/a_{\text{lens}}$), and the position angle of the lens (ϕ_{lens} ; degrees east of north). Unless otherwise stated, when optical or near-IR imaging suggests the presence of additional lenses (see Figure 3), we estimate centroids for each lens by-eye and fix the positions of the additional lenses with respect to the primary lens. Each additional lens thus has 3 free parameters: θ_E , q_{lens} , and ϕ_{lens} . We assume secondary, tertiary, etc., lenses are located at the same redshift as the primary lens.

The total number of free parameters for any given system is $N_{\text{free}} = 5 + 3 \times (N_{\text{lens}} - 1) + 6 * N_{\text{source}}$, where N_{source} is the number of Sérsic profiles used.

We use uniform priors for all model parameters. The prior on the position of the lenses covers $\pm 0''.6$ ($1''.0$) in both RA and Dec, a value that reflects the 1σ absolute astrometric solution between the ALMA and optical/near-IR images of $0''.2$ ($0''.4$) for SDSS-based (2MASS-based) astrometric calibration. In section ??, we discuss the level of agreement between the astrometry from the images and the astrometry from the lens modeling on an object-by-object basis. For θ_E , the prior covers $0''.1 - 6''$. The axial ratios of the lenses and sources are restricted to be $q_{\text{lens}} > 0.3$ and $q_s > 0.2$. No prior is placed on the position angle of the lens or source. The intrinsic flux density for any source is allowed to vary from 0.1 mJy to the total flux density observed by the ALMA. The source position is allowed to vary over any reasonable range necessary to fit the data (typically, this is $\pm 1 - 2''$). The effective radius is allowed to vary from $0''.01 - 1''.5$.

The surface brightness map generated as part of UVMCMCFIT is then converted to a “simulated visibility” dataset (V_{model}) in much the same way as MIRIAD’s UVMODEL routine. Indeed, the code used in UVMCMCFIT is a direct Python port of UVMODEL (the use of UVMODEL itself is not possible for the same reason as GRAVLENS: constant input/output makes parallel computing prohibitively expensive). UVMCMCFIT computes the Fourier transform of the surface brightness map and samples the resulting visibilities in a way that closely matches the sampling of the actual observed ALMA visibility dataset (V_{ALMA}).

The quality of fit for a given set of model parameters is determined from the maximum likelihood estimate MLE according to the following equation:

$$MLE = \sum_{u,v} \frac{|V_{\text{ALMA}} - V_{\text{model}}|^2}{\sigma^2} + \log(2\pi\sigma^2) \quad (1)$$

where σ is the 1σ uncertainty level for each visibility and is determined from the scatter in the visibilities within a single spectral window (this is a natural weighting scheme).

We use EMCEE (Foreman-Mackey et al. 2013) to sample the posterior probability density function (PDF) of our model parameters. EMCEE is a Markov chain Monte Carlo (MCMC) code that uses an affine-invariant ensemble sampler to obtain significant performance advantages over standard MCMC sampling methods (Goodman & Weare 2010).

We employ a “burn-in” phase with 512 walkers and

500-1000 iterations (i.e., $\approx 250,000 - 500,000$ samplings of the posterior PDF) to identify the best-fit model parameters. This position then serves as the basis to initialize the “final” phase with 512 walkers and 10 iterations (i.e., 5,120 samplings of the posterior PDF) to determine uncertainties on the best-fit model parameters.

During each MCMC iteration, we also measure the magnification factor at $870\mu\text{m}$, μ_{870} , for each source. This is done simply by taking the ratio of the total flux density in the lensed image of the model (S_{out}) to the total flux density in the unlensed, intrinsic source model (S_{in}). The use of an aperture when computing μ_{870} is important when source profiles are used with significant flux at large radii (e.g., some types of Sérsic profiles). For an elliptical Gaussian, such a step is unnecessary (note that we did test this and found only $\approx 10\%$ difference between μ_{870} computed with and without an aperture). The best-fit value and 1σ uncertainty on μ_{870} are drawn from the posterior PDF, as with the other parameters of the model.

3.2. Individual Model Fits

In this section, we present our model fits and describe each source in detail.

ADFS01: Three sources are detected by ALMA, each of which is weakly lensed by a bright foreground galaxy seen in the *HST* image. Alternative scenarios involving strong lensing can be ruled out by the location of the lens: $\approx 2 - 3''$ north of the centroid of the ALMA sources (the rms error in the astrometry is set from 2MASS at a level of $\approx 0''.5$) as well as the unusual location and fluxes of the ALMA sources relative to each other. We assume an Einstein radius of $0''.5$ and fix the position angle of the lens to be between 40-50 degrees to match the orientation seen in the *HST* image. Larger Einstein radii can be ruled out by the absence of counter images north of the lens.

ADFS02: Two sources are detected by ALMA, both of which are weakly lensed by a foreground galaxy in the *HST* image. The ALMA sources have the largest separation of any in our sample overall: $\approx 10''$. We assume an Einstein radius of $1''.5$ for the foreground lens as a “maximal lensing” scenario. This results in magnification factors of $\mu_{870} = 2.3 \pm 0.1$ and $\mu_{870} = 1.2 \pm 0.1$ for the two sources. Our constraints on the true Einstein radius of the lens are weak, so these values for μ_{870} should be regarded as upper limits.

ADFS03: Three sources are detected by ALMA, none of which appear to be lensed (the closest bright *HST* source is located $\approx 13''$ away from the ALMA sources).

ADFS04: Three sources are detected by ALMA. In this paper, we have assumed that all three are unlensed. There is a group of three sources detected in our Gemini-S optical imaging located $\approx 7''$ east of the ALMA sources. This distance is so large that plausible mass ranges for the Gemini-S sources would imply at most a factor of 1.1-1.2 boost in the apparent flux densities of the ALMA sources.

ADFS05: Two sources are detected by ALMA. The nearest possible lens is located $\approx 8''$ from the ALMA sources, indicating that lensing is likely to be irrelevant in this system. The two ALMA sources are similarly bright ($S_{870} = 8.27 \pm 0.53$ mJy and $S_{870} = 9.07 \pm 0.27$ mJy) and separated by $\approx 0''.8$, corresponding to a projected physical distance of ≈ 6 kpc. This distance is typical of

the pericentric passage distance in hydrodynamical simulations of major mergers (e.g., Hayward et al. 2012). A plausible scenario is that ADFS05 represents a major merger that just experienced a first pass which significantly enhanced star-formation in both sources.

ADFS06: Three sources are detected by ALMA, all of which are weakly lensed by a foreground galaxy seen in the *HST* image. We assume an Einstein radius of $0''.5$ for the lens, as values larger than this produce multiple images of the ALMA sources. Based on the brightness of the lens, we consider to be unlikely values for the Einstein radius that are smaller than $0''.5$, so the results we report for this object should be robust.

ADFS07: This is a single source that is strongly lensed by a foreground galaxy seen in the *HST* image. The lensed source is not detected by *HST*. The source is highly elongated ($q_s = 0.31 \pm 0.01$), but fits the data very well. The position of the lens according to the lens model is consistent with the position in the *HST* image given the $0''.5$ fundamental uncertainty due to using the 2MASS system as the fundamental basis for the astrometry.

ADFS_M0: Two sources are detected by ALMA, both of which are weakly lensed by a group of small galaxies detected in the *HST* image. We represent the gravitational potential of the group with a single SIE lens and an Einstein radius of $1''.0$. Values larger than this produce additional counter images that are not seen in the ALMA imaging. We cannot rule out smaller Einstein radii, but we consider these unlikely given the number of sources and their brightness in the *HST* image.

CDFS_M0: This is a complex, very well constrained system. Two sources are detected by ALMA: one is strongly lensed and the other is weakly lensed. In addition, the lens is detected by ALMA (this is one of two sources in the entire ALMA sample that is unresolved by ALMA). These facts work together to provide very tight constraints on the system. Since the lens is detected by ALMA, its position relative to the lensed images is unambiguous. Also, because there is a strongly lensed source with multiple images, the Einstein radius of the lens is unambiguous. A byproduct of these two facts is that the magnification factor of the weakly lensed source is known to very high precision as well. It experiences a magnification factor of $\mu_{870} = 1.520 \pm 0.002$ despite being located $\approx 4''$ north of the lens (which has an Einstein radius of 1.353 ± 0.005). We use these numbers to inform our estimates of the Einstein radius for weakly lensed sources without the excellent constraints provided by this system.

CDFS_M1: Two sources are detected by ALMA, both of which are weakly lensed by a foreground galaxy seen in the *HST* image. There is also a 3σ peak coincident with *HST* source that may be an indication that the lens has been detected by ALMA. We do not attempt to model this 3σ peak. We assume an Einstein radius of $0''.5$ for the lens, since larger values predict the existence of counter images that are not seen by ALMA. The second ALMA source is located $\approx 5''$ from the lens but still experiences a significant magnification of $\mu_{870} = 1.12 \pm 0.02$.

ECDFS02: This system is very similar to ADFS05, except that here the two ALMA sources are separated by $\approx 0''.4$ rather than $0''.8$ and one source is brighter than the other by a factor of 2. Assuming the two sources

have similar mass to light ratios, their brightness ratios indicate major merger rather than minor merger activity. The projected physical distance is $\approx 2 - 3$ kpc, assuming a redshift of $z = 2$ for the ALMA sources. This could be an example of a major merger approaching final coalescence and experiencing a significant boost in star-formation due to enhancements in the local gas density brought about by dynamical friction forces during the merger.

ElaisS1: Four sources are detected by ALMA, all of which are weakly lensed by a foreground galaxy seen in the *HST* image. We assume an Einstein radius of $1''.5$ for the lens as larger values begin to predict counter images that are not seen by ALMA. The magnification factors reported here should be regarded as upper limits since we do not have strong constraints on the lower limit of the Einstein radius of the lens (e.g., the magnification factor for the source that is directly south of the lens is reported here to have $\mu_{870} = 1.68 \pm 0.06$, but values as small as 1.1-1.2 are likely plausible as well).

COS01: This system is similar to ADFS07: a single source that is strongly lensed by a foreground galaxy seen in the *HST* image. In fact, the background source is also detected by *HST* as well as Keck/NIRC-II adaptive optics imaging, and a lens model has been published based on these data (Calanog et al. 2014). The morphology of the lensed emission is very different between the Keck and ALMA imaging, suggesting differential magnification is important in this object. The very small sizes of the sources are consistent with this as well ($r_s = 0.023 \pm 0.003''$, Keck and $r_s = 0.055 \pm 0.007''$, ALMA). Adopting a redshift of $z = 2$ for the lensed source implies physical sizes of ≈ 150 pc and ≈ 300 pc for the rest-frame optical and rest-frame far-IR, respectively.

COS02: Five sources are detected by ALMA, none of which appear to be lensed. This is one of two objects in our sample that have five ALMA counterparts. There are also a number of $2 - 3\sigma$ peaks in the map that could be real, further increasing the multiplicity rate for this object. However, there are also negative peaks of somewhat similar amplitude at a relatively high rate in this map, so we choose to be conservative in our assessment of what is a real source for this object. Some of the ALMA sources have counterparts detected in the *HST* image.

XMM01: Three sources are detected by ALMA, all of which are weakly lensed by two foreground galaxies seen in the *HST* and Keck/NIRC-II imaging. The ALMA imaging is broadly consistent with SMA data originally presented in Fu et al. (2013), with two bright sources and a much fainter third source very close to the more southern bright source. We assume Einstein radii of $0''.5$ for both lenses to reproduce the approach used in Fu et al. (2013). This results in magnification factors for the three sources of $\mu_{879} \approx 1.6 - 1.7$, similar to Fu et al. (2013).

XMM02: Two sources are detected by ALMA, both of which are weakly lensed. This system is similar to ADFS02, although the two ALMA sources are much closer and the lens must be less massive in order to avoid producing multiple images of the closest ALMA source. The fainter ALMA source has a much lower magnification factor than the brighter source ($\mu_{870} = 1.10 \pm 0.01$ vs. $\mu_{870} = 1.63 \pm 0.11$). As with ADFS02, we caution

that these magnification factors represent the “maximal lensing” scenario and hence should be considered upper limits.

XMM03: One source is detected by ALMA, and it is weakly lensed by two foreground galaxies seen in the *HST* images. We assume an Einstein radius of $1''$ for the foreground lenses and fix the positions of both lenses according to the location of the foreground galaxies in the *HST* image. As with XMM02, this is the “maximal lensing” scenario, so our magnification measurement of $\mu_{870} = 1.80 \pm 0.16$ should be considered an upper limit.

XMM04: Two sources are detected by ALMA, none of which appear to be lensed. The brighter ALMA source is weakly detected in the CFHT *i*-band image.

XMM05: One source is detected by ALMA, and it is weakly lensed by a group of foreground galaxies seen in the *HST* image. We assume an Einstein radius of $0''.2$ for the nearest lensing galaxy and allow a $\pm 0''.4$ shift in its position relative to that indicated by the *HST* image (which has its astrometry tied to SDSS). We represent the remaining members of the group as a single SIS located $4''.5$ south and $4''.5$ east of the image centroid and having an Einstein radius of $2''.0$. This is meant to represent the “maximal lensing” scenario, so our measurement of μ_{870} should be regarded as an upper limit. The presence of two 3σ peaks located near the center of the residual image indicates that the model does not fit the data perfectly. This could be an indication that either of our assumptions for the lens potential or source structure are oversimplifications. Higher resolution imaging is needed to determine the most likely cause.

XMM06: One source is detected by ALMA, and it is strongly lensed by one foreground galaxy seen in the *HST* image. The lensed source is not detected in the *HST* image. This object also has high quality SMA imaging and an accompanying lens model that produces consistent results with those given here (Bussmann et al. 2013).

XMM16: Three sources are detected by ALMA, all of which are weakly lensed by a foreground galaxy detected in the *HST* image and located $\approx 6''$ from the ALMA sources. The central source is much brighter than the other two sources, which makes fitting a model challenging. We forced the positions of the second and third sources to be at least $0''.5$ and $-0''.5$ away from the first source in declination, respectively. Furthermore, we fixed the position of the lens to be located $2''.5$ west and $0''.5$ south of the image centroid given in Table 1. We also fixed the Einstein radius to be $1''.0$, a typical value for isolated galaxies in this sample and in Bussmann et al. (2013). Because the source is so far from the lens, the magnification factor is only $\mu_{870} = 1.19 \pm 0.01$.

XMM101: One source is detected by ALMA, and it appears to be unlensed. A faint smudge seen in the *HST* image of this source is due to a star located $3''.5$ northeast of the ALMA source.

XMM102: Five sources are detected by ALMA, none of which appear to be lensed. There are a few faint smudges seen in the *HST* image which are likely to be the rest-frame optical counterparts to the ALMA sources. The ALMA sources are all arranged in a chain like shape, possibly suggestive of a larger filamentary overdensity in which they might reside.

XMM108: One source is detected by ALMA, and it is strongly lensed by one foreground galaxy detected

in the Gemini-S image. There is a $\approx 0''.5$ offset in the position of the foreground galaxy between the lens model and the Gemini-S image. Given the absolute astrometric uncertainty of $0''.2$ (based on SDSS), we do not consider this offset to be significant. The presence of a handful of $\pm 3\sigma$ peaks in the residual map is likely an indication that our assumption of a single Gaussian to describe the source morphology is an oversimplification.

XMM109: One source is detected by ALMA, and it is strongly lensed by one foreground galaxy detected in the Gemini-S image. As with XMM108, there is a $\approx 0''.5$ offset between the lens position according to the lens model and the Gemini-S image. We do not consider this offset significant. An alternative model in which the lens is sub-mm luminous cannot be ruled out, but we consider this unlikely for a number of reasons. First, it is a more complex model (having two sources and one lens, rather than one source and one lens). Second, lenses are very rarely detected in sub-mm imaging. Third, the shape and location of the ALMA sources relative to the Gemini-S source are typical of strongly lensed objects (consistent with the very low residuals). Fourth, the alternative lens model predicts the lensed source to have an intrinsic flux density of ≈ 13 mJy, which would make it the brightest source in the sample.

XMM110: Two sources are detected by ALMA, neither of which are lensed. The faint, diffuse emission seen in the CFHT *i*-band image is atypical of lensing galaxies. The nearest bright galaxy seen at *i*-band is located $\approx 18''$ southeast of the ALMA sources.

XMM115: One source is detected by ALMA, and it is weakly lensed by a foreground galaxy seen in the *HST* image. We assume an Einstein radius of $0''.5$ to represent the “maximal lensing” scenario. Due to the elliptical nature of the lens, this results in a magnification factor of $\mu_{870} = 3.72 \pm 0.42$. The *HST* morphology is complex: diffuse emission to the north of the lens could be a detection of the background source or could be a long spiral arm associated with the lensing galaxy.

XMM119: Two sources are detected by ALMA, both of which are weakly lensed by a foreground galaxy detected in the *HST* image. An Einstein radius of $1''.5$ is used to represent the “maximal lensing” scenario and results in magnification factors of $\mu_{870} = 2.25 \pm 0.17$ and $\mu_{870} = 1.48 \pm 0.09$.

XMM124: One source is detected by ALMA, and it is coincident (within the astrometric uncertainty) with a late-type galaxy seen in the *HST* image. Here, we assume that the *HST* source is the true counterpart to the ALMA source, implying that no lensing is occurring.

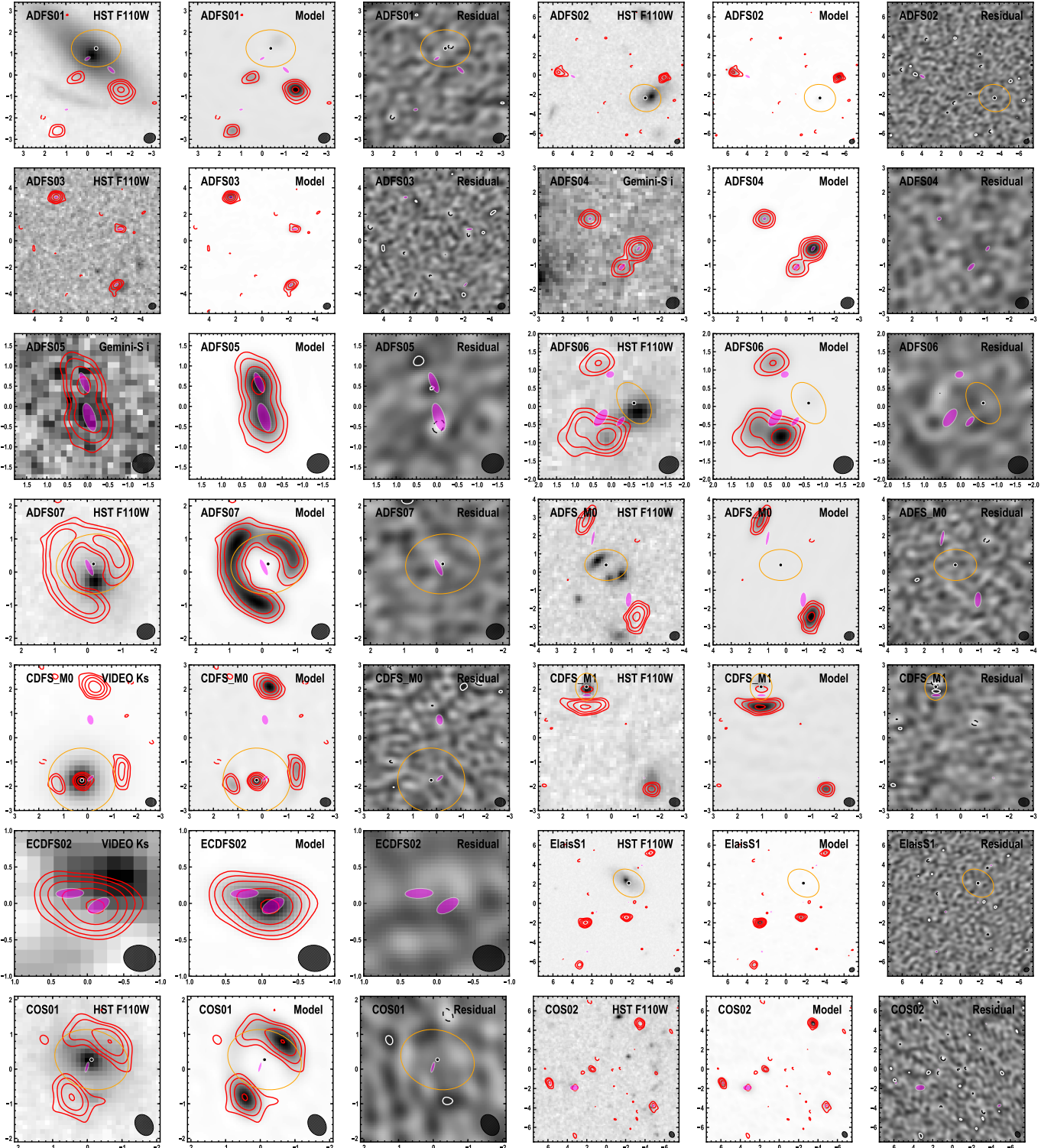


Figure 3. Model fits for each target in the ALMA sample, 3 panels per target. *Left:* ALMA 870 μ m imaging (red contours, starting at $\pm 3\sigma$ and increasing by factors of 2) overlaid on best available optical or near-IR imaging (grayscale, with telescope and filter printed in upper right corner). The location and morphology of all sources used in the model are represented by magenta ellipses. If a lens is present, its location is given by a black circle and its critical curve is traced by an orange line. The FWHM size of the ALMA synthesized beam is shown in the lower left corner of each panel. *Middle:* Same as *left*, but showing best-fit model in grayscale. *Right:* Same as *left*, but showing residual image obtained from subtracting best-fit model from the data.

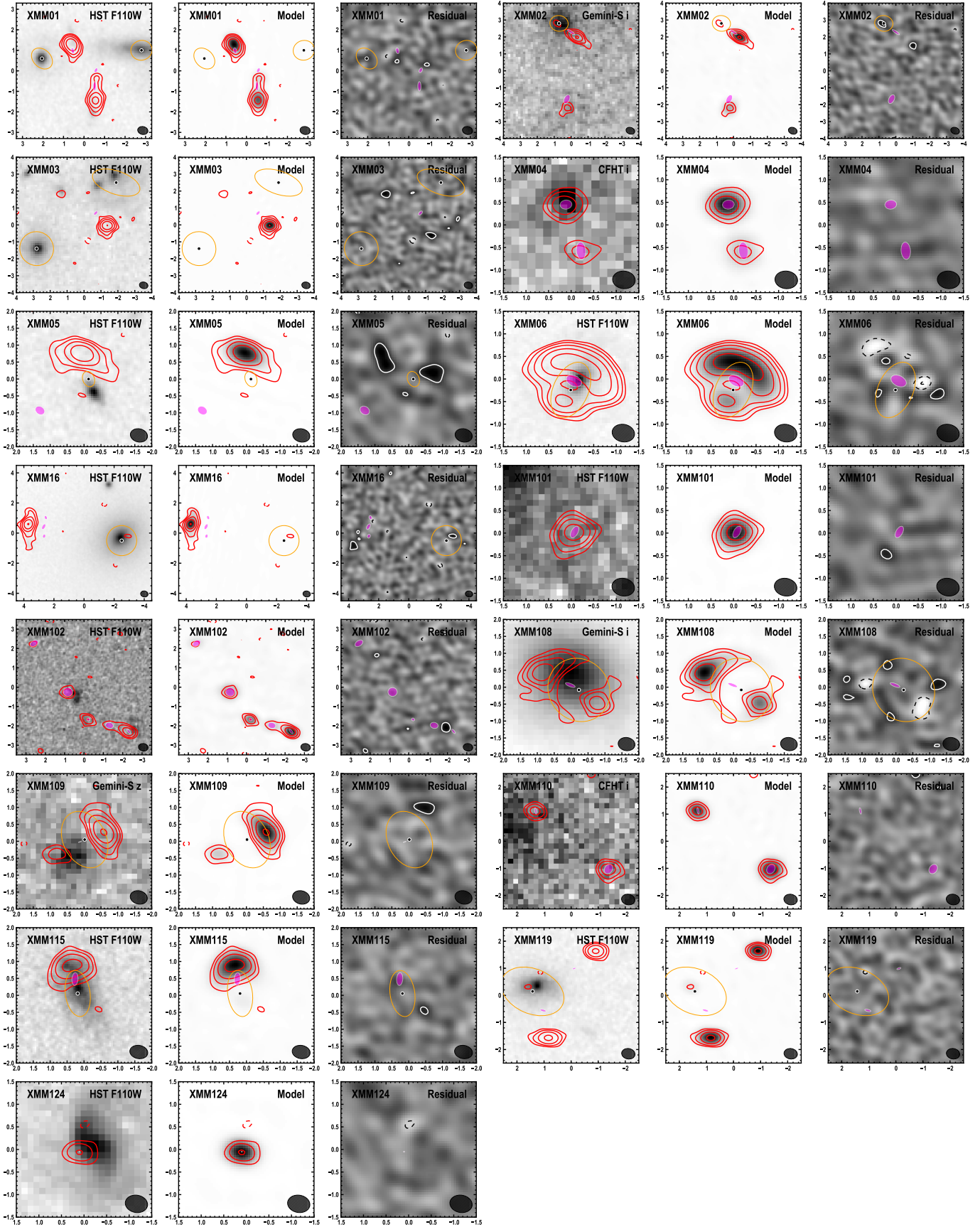
**Figure 3.** Continued.

Table 2
 Lens properties from parameters of model fits to ALMA sources. Parameters without uncertainties were fixed to the given value.

Short name	Lens ID	RA ₈₇₀ (J2000)	Dec ₈₇₀ (J2000)	σ_{RA} ($''$)	σ_{Dec} ($''$)	θ_E ($''$)	q_{lens}	ϕ_{lens} (deg)
ADFS01	Lens0	04:50:57.688	-53:16:53.10	0.005	0.06	1.0	0.707 ± 0.141	93 ± 7
ADFS02	Lens0	04:50:27.213	-52:41:27.73	0.004	0.06	1.5	0.897 ± 0.047	74 ± 18
ADFS06	Lens0	04:33:40.413	-54:03:39.39	0.009	0.07	0.5	0.662 ± 0.135	37 ± 12
ADFS07	Lens0	04:41:53.867	-54:03:53.23	0.001	0.01	1.006 ± 0.004	0.794 ± 0.008	99 ± 1
ADFS_M0	Lens0	04:38:30.910	-54:18:29.11	0.003	0.12	1.0	0.723 ± 0.068	82 ± 9
CDFS_M0	Lens0	03:27:52.025	-29:09:12.15	0.001	0.01	1.354 ± 0.006	0.955 ± 0.007	80 ± 6
CDFS_M1	Lens0	03:32:10.907	-27:05:32.09	0.002	0.01	0.5	0.807 ± 0.006	176 ± 3
COS01	Lens0	10:01:44.174	+02:57:12.75	0.001	0.02	0.956 ± 0.005	0.775 ± 0.025	72 ± 1
ElaisS1	Lens0	00:38:23.481	-43:37:01.90	0.013	0.19	1.5	0.790 ± 0.067	44 ± 6
XMM01	Lens0	02:20:16.746	-06:01:42.58	—	—	0.5	0.801 ± 0.062	48 ± 14
—	Lens1	02:20:16.423	-06:01:42.18	—	—	0.5	0.882 ± 0.072	90 ± 17
XMM02	Lens0	02:22:01.671	-03:33:38.45	0.008	0.10	0.5	0.706 ± 0.124	67 ± 11
XMM03	Lens0	02:25:48.129	-04:17:52.20	—	—	1.0	0.531 ± 0.180	45 ± 14
—	Lens1	02:25:47.815	-04:17:48.30	—	—	1.0	0.569 ± 0.197	67 ± 16
XMM05	Lens0	02:30:05.947	-03:41:53.35	0.005	0.06	0.519 ± 0.044	0.852 ± 0.097	24 ± 20
XMM06	Lens0	02:18:30.673	-05:31:31.99	0.001	0.01	0.507 ± 0.004	0.596 ± 0.009	157 ± 1
XMM108	Lens0	02:19:18.398	-03:10:51.31	0.002	0.13	0.928 ± 0.007	0.902 ± 0.024	26 ± 7
XMM109	Lens0	02:29:44.738	-03:41:09.52	0.002	0.01	0.743 ± 0.008	0.703 ± 0.050	26 ± 1
XMM115	Lens0	02:20:21.768	-01:53:30.88	0.002	0.03	0.5	0.547 ± 0.050	11 ± 6
XMM119	Lens0	02:20:29.234	-06:48:46.30	0.005	0.05	1.0	0.663 ± 0.094	64 ± 6

Table 3

Intrinsic properties from parameters of model fits to ALMA sources.
 Uncertainties in flux densities do not include absolute calibration uncertainty
 of $\approx 10\%$.

Short name	Source ID	ΔRA_{870} (J2000)	ΔDec_{870} (J2000)	S_{870} (mJy)	r_s ($''$)	q_s	ϕ_s (deg)	μ_{870}
ADFS01	Source0	-0.734 ± 0.069	-1.070 ± 0.053	4.32 ± 0.28	0.112 ± 0.006	0.41 ± 0.05	45 ± 3	1.64 ± 0.10
ADFS01	Source1	1.415 ± 0.056	-2.912 ± 0.059	1.49 ± 0.11	0.059 ± 0.018	0.54 ± 0.12	94 ± 48	1.26 ± 0.03
ADFS01	Source2	0.427 ± 0.055	-0.514 ± 0.059	0.83 ± 0.13	0.084 ± 0.020	0.50 ± 0.13	125 ± 14	2.72 ± 0.33
ADFS02	Source0	-0.868 ± 0.050	0.938 ± 0.048	2.54 ± 0.18	0.055 ± 0.010	0.83 ± 0.09	131 ± 20	2.29 ± 0.13
ADFS02	Source1	7.496 ± 0.058	2.190 ± 0.059	3.72 ± 0.20	0.179 ± 0.012	0.59 ± 0.08	63 ± 6	1.20 ± 0.01
ADFS03	Source0	2.343 ± 0.007	3.284 ± 0.005	7.50 ± 0.24	0.109 ± 0.008	0.70 ± 0.11	92 ± 14	1.00 ± 0.00
ADFS03	Source1	-2.191 ± 0.013	-3.320 ± 0.011	3.84 ± 0.27	0.099 ± 0.019	0.53 ± 0.17	135 ± 24	1.00 ± 0.00
ADFS03	Source2	-2.503 ± 0.035	0.886 ± 0.019	2.06 ± 0.30	0.122 ± 0.040	0.51 ± 0.17	89 ± 20	1.00 ± 0.00
ADFS04	Source0	-1.126 ± 0.005	-0.319 ± 0.004	8.65 ± 0.23	0.073 ± 0.010	0.67 ± 0.15	133 ± 24	1.00 ± 0.00
ADFS04	Source1	0.876 ± 0.011	0.908 ± 0.009	3.53 ± 0.18	0.048 ± 0.019	0.71 ± 0.19	84 ± 43	1.00 ± 0.00
ADFS04	Source2	-0.437 ± 0.017	-1.088 ± 0.016	2.76 ± 0.16	0.093 ± 0.020	0.58 ± 0.20	131 ± 38	1.00 ± 0.00
ADFS05	Source0	0.067 ± 0.008	0.588 ± 0.015	7.02 ± 0.42	0.136 ± 0.012	0.38 ± 0.06	23 ± 5	1.00 ± 0.00
ADFS05	Source1	-0.060 ± 0.009	-0.268 ± 0.018	8.27 ± 0.53	0.193 ± 0.015	0.42 ± 0.06	17 ± 4	1.00 ± 0.00
ADFS06	Source0	0.333 ± 0.101	-0.513 ± 0.040	5.14 ± 0.39	0.091 ± 0.006	0.39 ± 0.05	142 ± 4	1.70 ± 0.14
ADFS06	Source1	0.865 ± 0.123	-0.420 ± 0.041	4.09 ± 0.29	0.165 ± 0.013	0.43 ± 0.06	141 ± 4	1.42 ± 0.07
ADFS06	Source2	0.604 ± 0.108	0.739 ± 0.077	1.56 ± 0.20	0.077 ± 0.015	0.75 ± 0.16	101 ± 40	1.79 ± 0.18
ADFS07	Source0	0.131 ± 0.005	-0.105 ± 0.006	3.28 ± 0.13	0.128 ± 0.005	0.30 ± 0.01	24 ± 1	9.81 ± 0.31
ADFS_M0	Source0	-1.340 ± 0.043	-1.816 ± 0.119	9.81 ± 0.33	0.225 ± 0.006	0.46 ± 0.02	178 ± 1	1.43 ± 0.03
ADFS_M0	Source1	0.658 ± 0.039	1.569 ± 0.111	4.27 ± 0.24	0.180 ± 0.010	0.25 ± 0.02	167 ± 2	1.52 ± 0.07
CDFS_M0	Source0	-0.348 ± 0.006	0.077 ± 0.004	1.58 ± 0.06	0.085 ± 0.004	0.38 ± 0.03	134 ± 3	8.29 ± 0.19
CDFS_M0	Source1	-0.342 ± 0.005	2.489 ± 0.008	9.37 ± 0.14	0.147 ± 0.003	0.65 ± 0.02	14 ± 2	1.52 ± 0.00
CDFS_M0	Source0	0.000 ± 0.000	0.000 ± 0.000	5.83 ± 0.11	0.026 ± 0.009	0.79 ± 0.15	85 ± 63	1.00 ± 0.00
CDFS_M1	Source0	-0.011 ± 0.011	-0.347 ± 0.004	3.71 ± 0.09	0.096 ± 0.005	0.35 ± 0.03	91 ± 2	2.95 ± 0.04
CDFS_M1	Source1	-2.366 ± 0.024	-3.752 ± 0.007	2.26 ± 0.10	0.032 ± 0.012	0.68 ± 0.19	93 ± 55	1.12 ± 0.02
COS01	Source0	0.136 ± 0.011	-0.220 ± 0.016	1.35 ± 0.13	0.068 ± 0.006	0.27 ± 0.04	164 ± 2	9.44 ± 0.95
COS02	Source0	-3.507 ± 0.012	4.659 ± 0.013	3.31 ± 0.16	0.073 ± 0.017	0.70 ± 0.12	94 ± 34	1.00 ± 0.00
COS02	Source1	5.780 ± 0.019	-1.434 ± 0.026	2.26 ± 0.19	0.094 ± 0.029	0.76 ± 0.13	106 ± 65	1.00 ± 0.00
COS02	Source2	-4.869 ± 0.049	-3.769 ± 0.050	1.54 ± 0.23	0.198 ± 0.051	0.65 ± 0.13	72 ± 41	1.00 ± 0.00
COS02	Source3	1.410 ± 0.031	-0.035 ± 0.033	1.45 ± 0.18	0.101 ± 0.042	0.71 ± 0.13	74 ± 42	1.00 ± 0.00
COS02	Source4	3.301 ± 0.083	-1.864 ± 0.060	1.80 ± 0.33	0.312 ± 0.060	0.67 ± 0.13	78 ± 32	1.00 ± 0.00
ECDFS02	Source0	-0.156 ± 0.011	-0.034 ± 0.011	9.30 ± 1.20	0.099 ± 0.012	0.52 ± 0.12	123 ± 7	1.00 ± 0.00
ECDFS02	Source1	0.221 ± 0.061	0.127 ± 0.018	4.83 ± 1.26	0.109 ± 0.024	0.38 ± 0.08	88 ± 7	1.00 ± 0.00
Elaiss1	Source0	3.113 ± 0.160	-3.112 ± 0.155	6.94 ± 0.17	0.096 ± 0.005	0.80 ± 0.05	91 ± 6	1.29 ± 0.02
Elaiss1	Source1	-0.111 ± 0.114	-2.172 ± 0.183	2.46 ± 0.12	0.065 ± 0.008	0.84 ± 0.05	87 ± 7	1.68 ± 0.06
Elaiss1	Source2	-1.470 ± 0.158	1.774 ± 0.145	1.55 ± 0.13	0.105 ± 0.016	0.86 ± 0.04	120 ± 7	1.53 ± 0.04
Elaiss1	Source3	4.039 ± 0.165	-7.216 ± 0.174	1.57 ± 0.13	0.124 ± 0.020	0.79 ± 0.05	77 ± 7	1.16 ± 0.01
XMM01	Source0	-1.503 ± 0.013	0.395 ± 0.017	8.68 ± 0.26	0.090 ± 0.005	0.56 ± 0.06	12 ± 19	1.77 ± 0.04
XMM01	Source1	-2.563 ± 0.018	-1.337 ± 0.017	7.91 ± 0.23	0.116 ± 0.006	0.34 ± 0.03	2 ± 1	1.42 ± 0.01
XMM01	Source2	-2.622 ± 0.025	-0.552 ± 0.025	1.15 ± 0.16	0.077 ± 0.025	0.66 ± 0.18	134 ± 33	1.58 ± 0.06
XMM02	Source0	-0.844 ± 0.111	-0.648 ± 0.081	4.97 ± 0.35	0.106 ± 0.007	0.26 ± 0.03	54 ± 2	1.63 ± 0.11
XMM02	Source1	-0.596 ± 0.122	-4.592 ± 0.098	2.97 ± 0.31	0.168 ± 0.023	0.59 ± 0.16	139 ± 41	1.10 ± 0.01
XMM03	Source0	-3.505 ± 0.094	1.937 ± 0.081	7.86 ± 0.74	0.095 ± 0.006	0.59 ± 0.06	142 ± 5	1.80 ± 0.16
XMM04	Source0	0.114 ± 0.009	0.451 ± 0.008	5.46 ± 0.30	0.088 ± 0.012	0.82 ± 0.14	90 ± 44	1.00 ± 0.00
XMM04	Source1	-0.236 ± 0.034	-0.562 ± 0.030	1.78 ± 0.37	0.116 ± 0.051	0.70 ± 0.20	88 ± 55	1.00 ± 0.00
XMM05	Source0	0.059 ± 0.040	0.567 ± 0.032	7.58 ± 0.74	0.111 ± 0.006	0.52 ± 0.04	36 ± 5	2.15 ± 0.23
XMM06	Source0	-0.278 ± 0.008	0.239 ± 0.011	11.66 ± 0.45	0.122 ± 0.003	0.64 ± 0.02	62 ± 2	5.33 ± 0.19
XMM16	Source0	5.180 ± 0.003	0.923 ± 0.003	15.42 ± 0.43	0.129 ± 0.004	0.51 ± 0.03	-23 ± 2	1.19 ± 0.01
XMM16	Source1	5.159 ± 0.027	2.068 ± 0.029	1.66 ± 0.17	0.089 ± 0.011	0.75 ± 0.12	18 ± 31	1.19 ± 0.01
XMM16	Source2	5.125 ± 0.046	0.286 ± 0.229	1.12 ± 0.15	0.088 ± 0.015	0.76 ± 0.11	-8 ± 41	1.19 ± 0.01
XMM101	Source0	-0.076 ± 0.004	0.024 ± 0.004	8.77 ± 0.24	0.085 ± 0.010	0.52 ± 0.11	152 ± 6	1.00 ± 0.00
XMM102	Source0	-2.308 ± 0.012	-2.275 ± 0.011	5.15 ± 0.32	0.089 ± 0.014	0.63 ± 0.16	58 ± 27	1.00 ± 0.00
XMM102	Source1	0.828 ± 0.025	-0.278 ± 0.023	3.31 ± 0.39	0.137 ± 0.026	0.84 ± 0.10	74 ± 44	1.00 ± 0.00
XMM102	Source2	-0.211 ± 0.017	-1.647 ± 0.014	2.88 ± 0.22	0.058 ± 0.020	0.80 ± 0.13	84 ± 45	1.00 ± 0.00
XMM102	Source3	-1.505 ± 0.157	-1.981 ± 0.064	1.94 ± 0.37	0.283 ± 0.198	0.67 ± 0.17	81 ± 21	1.00 ± 0.00
XMM102	Source4	2.588 ± 0.155	2.611 ± 0.218	0.94 ± 0.18	0.459 ± 0.246	0.58 ± 0.15	96 ± 51	1.00 ± 0.00
XMM108	Source0	0.016 ± 0.238	-0.016 ± 0.283	3.49 ± 0.46	0.074 ± 0.007	0.32 ± 0.02	66 ± 2	8.49 ± 1.13
XMM109	Source0	0.153 ± 0.024	-0.073 ± 0.011	0.85 ± 0.13	0.019 ± 0.003	0.20 ± 0.00	109 ± 1	27.15 ± 4.61
XMM110	Source0	-1.380 ± 0.010	-1.025 ± 0.010	6.31 ± 0.34	0.141 ± 0.011	0.80 ± 0.12	134 ± 36	1.00 ± 0.00
XMM110	Source1	1.311 ± 0.011	1.124 ± 0.010	3.81 ± 0.25	0.070 ± 0.018	0.59 ± 0.22	52 ± 56	1.00 ± 0.00
XMM115	Source0	0.095 ± 0.021	0.442 ± 0.025	5.13 ± 0.61	0.117 ± 0.007	0.52 ± 0.07	-2 ± 5	3.72 ± 0.42
XMM119	Source0	-0.392 ± 0.039	-0.740 ± 0.051	3.83 ± 0.29	0.064 ± 0.006	0.42 ± 0.06	75 ± 5	2.25 ± 0.17
XMM119	Source1	-1.507 ± 0.073	0.805 ± 0.053	4.21 ± 0.17	0.033 ± 0.010	0.46 ± 0.18	116 ± 14	1.48 ± 0.03
XMM124	Source0	0.101 ± 0.011	-0.050 ± 0.009	2.75 ± 0.14	0.020 ± 0.008	0.68 ± 0.20	89 ± 49	1.00 ± 0.00

The combination of our optical or near-IR imaging and our deep, high-resolution ALMA imaging permits us to map the foreground structure along the line of sight to the ALMA sources. With such maps in hand for all of our targets, we can estimate the impact that lensing has

4. RESULTS

4.1. De-lensing the ALMA Sample

on the intrinsic properties of the ALMA sources. In other words, we can “de-lens” the ALMA sample.

Figure 3 shows the observed (i.e., apparent) and intrinsic (i.e., de-lensed) distributions of S_{870} , r_s , angular separation, and q_s . Here, angular separation is the angular distance between an ALMA source and the centroid of all the ALMA sources for a given *Herschel* DSFG. Lensing has the strongest effect on S_{870} : the median flux density in the ALMA sample drops by a factor of 1.6 when lensing is taken into account, and a two-sided Kolmogorov-Smirnov (KS) test yields a p -value of 0.044. Even if strongly lensed sources are removed from the sample, the median intrinsic flux density is 1.3 times lower than the median apparent flux density. If we only consider examples of weak lensing (i.e., removing the unlensed sources), the factor rises back to 1.6. These factors will be significant sources of error if they are incorrectly ignored. When discussing the intrinsic properties of bright sources discovered in wide-field far-IR or mm surveys, it is critical to disentangle the effects of lensing.

The effect on the other source parameters (r_s , angular separation, and q_s) is less pronounced. The median source size decreases by a factor of 1.2 in the ALMA sample after accounting for lensing, but the two-sided KS test reveals a p -value of 0.174, suggesting that we cannot rule out the null hypothesis that both size distributions were drawn from the same parent distribution. We find no significant difference between the axial ratios of the apparent and intrinsic distributions as well as between the angular separations of apparent and intrinsic distributions (two-sided KS test p -values of 0.984 and 0.920, respectively).

It is worth noting that some of the effect of lensing is washed out by the presence of unlensed sources and strongly lensed sources in the ALMA sample. In both of these cases we assign the same value for axial ratio, angular separation, and size between the apparent and intrinsic distributions. If only weakly lensed sources are considered, the two-sided KS test p -values are 0.002, 0.039, and 0.304, respectively. There is a factor of 1.4, 1.3, and 1.2 difference in the median values for these three parameters between the apparent and intrinsic distributions. It is something of a surprise that axial ratios are on average lower in the intrinsic distribution. Observations at higher spatial resolution are needed to determine if this distinction is real.

Finally, the brightest single source in the ALMA sample is XMM06, with an intrinsic flux density of $S_{870} = 11.66 \pm 0.45$ mJy. However, there are also a number of sources with separations smaller than 1'' that have summed flux densities larger than this, including ADFS05, ECDFS02, XMM05, and XMM16. These sources have summed flux densities in the range $\approx 14 - 18$ mJy. The high end of this range is approaching the value of GN20 (20.6 mJy, Pope et al. 2006), a level that is extremely difficult for theorists to reproduce in simulations (e.g., Narayanan et al. 2010).

4.2. Multiplicity in the ALMA Sample

The second key result from our deep, high-resolution ALMA imaging is a firm measurement of the rate of multiplicity in *Herschel* DSFGs. We find that 20/29 *Herschel* DSFGs break down into multiple ALMA sources. Four out of these 20 comprise ALMA sources that are

separated by $< 1''$ and could be gravitationally bound systems (ADFS05, ECDFS02, XMM05, and XMM16). Depending on whether these 4 are considered multiples or not, the multiplicity rate in the ALMA sample is 55% - 69%. On the other hand, 5/9 of the single-component systems are strongly lensed. If these five are not considered, then the multiplicity rate increases to 64% - 80%.

In comparison, 69 DSFGs in the MAIN ALESS catalog show a multiplicity rate of 35% - 40% (Hodge et al. 2013). Smoothing our ALMA images and adding noise to match the resolution and sensitivity of ALESS results in a multiplicity rate of 55% (the 4 objects with sources that are separated by $< 1''$ become single systems). The redshift distributions for sources selected at S_{500} and S_{870} are expected to be very similar, with only a slightly higher median redshift for the ALESS sample (e.g., $z_{\text{med}} = 2.0$ vs. $z_{\text{med}} = 2.2$; see Zavala et al. 2014). In contrast, the ALESS sources are much fainter overall, having a median $870 \mu\text{m}$ flux density of $S_{870} \approx 6$ mJy compared to $S_{870} = 14.9$ mJy in our ALMA sample. Thus, the evidence favors brighter sources having a higher multiplicity rate. This result is also consistent with multiplicity studies of S_{870} -selected DSFGs by Smolčić et al. (2012) and Barger et al. (2012), who use PdBI/1.1 mm and SMA/870 μm imaging to determine rates of 22% and 40%, respectively.

One useful way to characterize multiplicity is with a comparison of the total $870 \mu\text{m}$ flux density, S_{total} , with the individual component $870 \mu\text{m}$ flux density, $S_{\text{component}}$. Figure 4 shows these values for our ALMA sample and compares to ALESS. Lensing has a significant impact on the apparent flux densities of many objects in our ALMA sample, so we are careful to show only intrinsic flux densities in this diagram. This diagram reflects the known result that the multiplicity rate in ALESS rises and the average fractional contribution per component ($\langle S_{\text{component}}/S_{\text{total}} \rangle$) decreases with increasing S_{total} (Hodge et al. 2013). A simple extrapolation of this phenomenon to the flux density regime probed by our ALMA sample would have suggested a very high multiplicity rate and a very low $\langle S_{\text{component}}/S_{\text{total}} \rangle$. We do find a higher multiplicity rate, but we find that $\langle S_{\text{component}}/S_{\text{total}} \rangle$ hovers around 0.4 for essentially the full range in our sample. In other words, the brightest *Herschel* DSFGs comprise 1-3 ALMA components, not 5-10 ALMA components as might have been expected from a naive extrapolation of the ALESS results.

We can dig further into our ALMA data by exploring the average number of ALMA sources per annular area (dN/dA) as a function of how apart they are from each other. Figure 5 shows the results of this analysis for both our ALMA sample and ALESS. We formulate the separation as an angular distance between each ALMA source and the centroid of all of the ALMA sources for that *Herschel* DSFG. This is different from Hodge et al. (2013), who use a simple pairwise separation distance estimator, a method that becomes ill-defined when there are more than 2 ALMA counterparts (as is often the case in our ALMA sample). Figure 5 shows dN/dA values for ALESS that have been re-computed using our method. We also show the median and 1σ range found from simulated datasets for both ALESS and our ALMA sample. The simulated datasets consist of 200 runs of DSFGs with the same flux density and multiplicity as

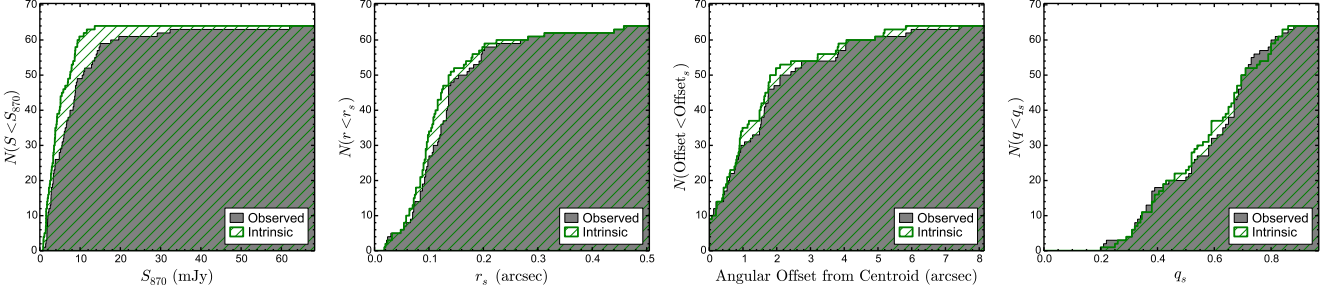


Figure 3. Cumulative distribution functions showing the effect of lensing on the inferred properties of the ALMA sample, including: flux densities (far left panel), effective radii (middle left panel), angular separation from centroid (middle right panel), and axial ratio (far right panel). The median flux density in the ALMA sample drops by a factor of 1.6 when lensing is taken into account. Lensing has a weaker (but still significant) impact on the effective radii and angular separation distributions, but the axial ratio distributions are statistically indistinguishable.

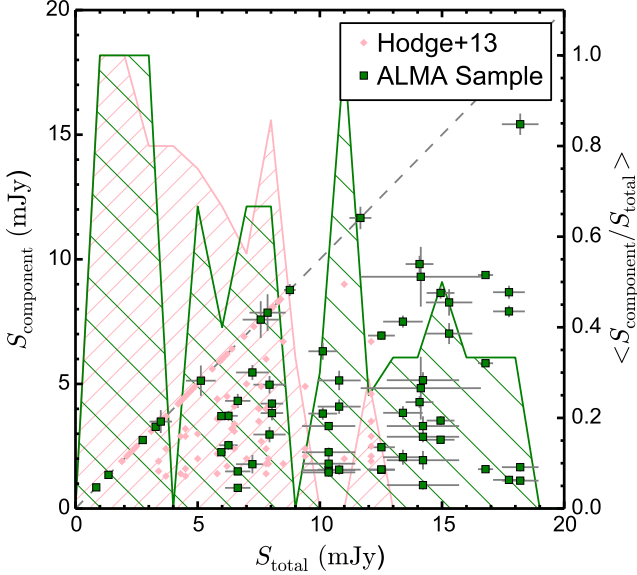


Figure 4. Comparison of the total $870\mu\text{m}$ flux density, S_{total} , with the individual component $870\mu\text{m}$ flux density, $S_{\text{component}}$ (both of these are after accounting for lensing). Objects falling along the gray dashed line are single component systems (i.e., $S_{\text{total}} = S_{\text{component}}$). The solid lines trace the average ratio of component to total flux for a given total flux. Our sample of *Herschel* DSFGs (ALMA sample, green squares) has a higher multiplicity and a lower $\langle S_{\text{component}}/S_{\text{total}} \rangle$ than the ALESS sample (pink diamonds). This result is consistent with trends within the ALESS sample alone, but the amplitude of the variation is not as large as expected.

the observed datasets (both the ALESS sample and our ALMA sample), but placed randomly within the primary beam FWHM.

We recover the result from Hodge et al. (2013) that the ALESS DSFGs are consistent with a uniformly distributed population. Interestingly, however, there is a dramatic rise in dN/dA for angular separations less than $2''$ in our ALMA sample. Indeed, for an angular separation of $0''.5$, we find an excess in dN/dA by a factor of > 5 compared to a random, uniformly distributed population. This may be a sign that it is only on size scales of $< 2''$ that excess number densities appear. Alternatively, it could be an indication that only the brightest DSFGs show an excess on small separation scales. Either way, this is important evidence that mergers play a key role in the evolution of the brightest DSFGs.

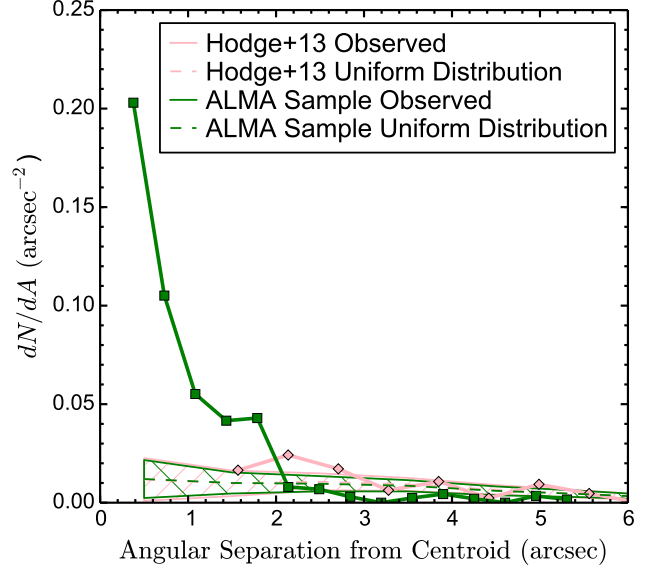


Figure 5. Number of ALMA sources per annular area as a function of angular separation from the ALMA centroid. Results are shown for our ALMA sample (thick green line) and ALESS (thick pink line) as well as simulated datasets based on each sample (thin green and thin pink hatched regions, respectively). We use a different method for computing angular separation from Hodge et al. (2013), but we reproduce their result that ALESS DSFGs are consistent with a randomly distribution population. On the other hand, the DSFGs in our ALMA sample show a very strong excess on angular separation scales $< 2''$. This is likely an indication that mergers play a key role in a significant fraction of the brightest DSFGs.

5. IMPLICATIONS FOR THE BRIGHT END OF THE DSFG LUMINOSITY FUNCTION

6. CONCLUSIONS

The results described in this paper are based on observations obtained with *Herschel*, an ESA space observatory with science instruments provided by European-led Principal Investigator consortia and with important participation from NASA.

This research has made use of data from the HerMES project (<http://hermes.sussex.ac.uk/>). HerMES is a Herschel Key Programme utilizing Guaranteed Time from the SPIRE instrument team, ESAC scientists, and a mission scientist. HerMES is described in Oliver et al. (2012). The HerMES data presented in this paper will be released through the *Herschel* Database in Marseille

(HeDaM⁶).

SPIRE has been developed by a consortium of institutes led by Cardiff Univ. (UK) and including: Univ. Lethbridge (Canada); NAOC (China); CEA, LAM (France); IFSI, Univ. Padua (Italy); IAC (Spain); Stockholm Observatory (Sweden); Imperial College London, RAL, UCL-MSSL, UKATC, Univ. Sussex (UK); and Caltech, JPL, NHSC, Univ. Colorado (USA). This development has been supported by national funding agencies: CSA (Canada); NAOC (China); CEA, CNES, CNRS (France); ASI (Italy); MCINN (Spain); SNSB (Sweden); STFC, UKSA (UK); and NASA (USA).

Based on observations obtained at the Gemini Observatory, which is operated by the Association of Universities for Research in Astronomy, Inc., under a cooperative agreement with the NSF on behalf of the Gemini partnership: the National Science Foundation (United States), the National Research Council (Canada), CONICYT (Chile), the Australian Research Council (Australia), Ministério da Ciência, Tecnologia e Inovação (Brazil) and Ministerio de Ciencia, Tecnología e Innovación Productiva (Argentina).

Facilities: ALMA, Gemini-S.

REFERENCES

- Barger, A. J., Wang, W.-H., Cowie, L. L., Owen, F. N., Chen, C.-C., & Williams, J. P. 2012, ApJ, 761, 89
- Becker, R. H., White, R. L., & Helfand, D. J. 1995, ApJ, 450, 559
- Blain, A. W. 1996, MNRAS, 283, 1340
- Bussmann, R. S., Gurwell, M. A., Fu, H., Smith, D. J. B., Dye, S., Auld, R., Baes, M., Baker, A. J., Bonfield, D., Cava, A., Clements, D. L., Cooray, A., Coppin, K., Dannerbauer, H., Dariush, A., De Zotti, G., Dunne, L., Eales, S., Fritz, J., Hopwood, R., Ibar, E., Ivison, R. J., Jarvis, M. J., Kim, S., Leeuw, L. L., Maddox, S., Michałowski, M. J., Negrello, M., Pascale, E., Pohlen, M., Riechers, D. A., Rigby, E., Scott, D., Temi, P., Van der Werf, P. P., Wardlow, J., Wilner, D., & Verma, A. 2012, ApJ, 756
- Bussmann, R. S., Pérez-Fournon, I., Amber, S., Calanog, J., Gurwell, M. A., Dannerbauer, H., De Bernardis, F., Fu, H., Harris, A. I., Krips, M., Lapi, A., Maiolino, R., Omont, A., Riechers, D., Wardlow, J., Baker, A. J., Birkinshaw, M., Bock, J., Bourne, N., Clements, D. L., Cooray, A., De Zotti, G., Dunne, L., Dye, S., Eales, S., Farrah, D., Gavazzi, R., González Nuevo, J., Hopwood, R., Ibar, E., Ivison, R. J., Laporte, N., Maddox, S., Martínez-Navajas, P., Michałowski, M., Negrello, M., Oliver, S. J., Roseboom, I. G., Scott, D., Serjeant, S., Smith, A. J., Smith, M., Streblyanska, A., Valiante, E., van der Werf, P., Verma, A., Vieira, J. D., Wang, L., & Wilner, D. 2013, ApJ, 779, 25
- Calanog, J. A., Fu, H., Cooray, A., Wardlow, J., Ma, B., Amber, S., Baes, M., Bock, J., Bourne, N., Bussmann, R. S., Casey, C. M., Chapman, S. C., Clements, D. L., Conley, A., Dannerbauer, H., DeZotti, G., Dunne, L., Dye, S., Eales, S., Farrah, D., Furlanetto, C., Harris, A. I., Ivison, R. J., Maddox, S. J., Magdis, G., Michałowski, M. J., Negrello, M., Nightingale, J., O'Bryan, J. M., Oliver, S. J., Riechers, D., Scott, D., Serjeant, S., Simpson, J., Smith, M., Timmons, N., Thacker, C., Valiante, E., & Vieira, J. D. 2014, ArXiv e-prints
- Chapman, S. C., Blain, A. W., Smail, I., & Ivison, R. J. 2005, ApJ, 622, 772
- Diolaiti, E., Bendinelli, O., Bonaccini, D., Close, L. M., Currie, D. G., & Parmeggiani, G. 2000, in Society of Photo-Optical Instrumentation Engineers (SPIE) Conference Series, Vol. 4007, Society of Photo-Optical Instrumentation Engineers (SPIE) Conference Series, ed. P. L. Wizinowich, 879–888
- Eales, S. et al. 2010, PASP, 122, 499
- Foreman-Mackey, D., Hogg, D. W., Lang, D., & Goodman, J. 2013, PASP, 125, 306
- Fu, H. et al. 2013, Nature, 498, 338
- Goodman, J. & Weare, J. 2010, Communications in Applied Mathematics and Computational Science, 5, 65
- Griffin, M. J. et al. 2010, A&A, 518, L3+
- Hayward, C. C., Jonsson, P., Kereš, D., Magnelli, B., Hernquist, L., & Cox, T. J. 2012, MNRAS, 424, 951
- Hezaveh, Y. D. et al. 2013, ApJ, 767, 132
- Ho, P. T. P., Moran, J. M., & Lo, K. Y. 2004, ApJ, 616, L1
- Hodge, J. A. et al. 2013, ApJ, 768, 91
- Hook, I. M., Jørgensen, I., Allington-Smith, J. R., Davies, R. L., Metcalfe, N., Murowinski, R. G., & Crampton, D. 2004, PASP, 116, 425
- Ivison, R. J. et al. 2013, ApJ, 772, 137
- Keeton, C. R. 2001, ArXiv Astrophysics e-prints
- Le Floc'h, E. et al. 2005, ApJ, 632, 169
- Madau, P., Ferguson, H. C., Dickinson, M. E., Giavalisco, M., Steidel, C. C., & Fruchter, A. 1996, MNRAS, 283, 1388
- Narayanan, D., Hayward, C. C., Cox, T. J., Hernquist, L., Jonsson, P., Younger, J. D., & Groves, B. 2010, MNRAS, 401, 1613
- Negrello, M., Perrotta, F., González-Nuevo, J., Silva, L., de Zotti, G., Granato, G. L., Baccigalupi, C., & Danese, L. 2007, MNRAS, 377, 1557
- Negrello, M. et al. 2010, Science, 330, 800
- Nguyen, H. T. et al. 2010, A&A, 518, L5
- Oliver, S. J. et al. 2012, MNRAS, 424, 1614
- Pilbratt, G. L. et al. 2010, A&A, 518, L1
- Pope, A. et al. 2006, MNRAS, 370, 1185
- Roseboom, I. G. et al. 2010, MNRAS, 409, 48
- Sersic, J. L. 1968, Atlas de galaxias australes (Cordoba, Argentina: Observatorio Astronomico, 1968)
- Smolčić, V., Aravena, M., Navarrete, F., Schinnerer, E., Riechers, D. A., Bertoldi, F., Feruglio, C., Finoguenov, A., Salvato, M., Sargent, M., McCracken, H. J., Albrecht, M., Karim, A., Capak, P., Carilli, C. L., Cappelluti, N., Elvis, M., Ilbert, O., Kartaltepe, J., Lilly, S., Sanders, D., Sheth, K., Scoville, N. Z., & Taniguchi, Y. 2012, A&A, 548, A4
- Treu, T. 2010, ARA&A, 48, 87
- Wardlow, J. L. et al. 2013, ApJ, 762, 59
- Zavala, J. A., Arétxaga, I., & Hughes, D. H. 2014, MNRAS, 443, 2384

⁶ <http://hedam.oamp.fr/HerMES>